ACS APPLIED MATERIALS & INTERFACES

www.acsami.org
Research Article

Transfection Potency of Lipid Nanoparticles Containing mRNA Depends on Relative Loading Levels

Suiyang Liao, Shuangyu Wang, Abishek Wadhwa, Alexandra Birkenshaw, Kevin Fox, Miffy Hok Yan Cheng, Irafasha C. Casmil, Armando Alcazar Magana, Nuthan Vikas Bathula, Chia Hao Ho, Jin-Yu Cheng, Leonard J. Foster, Kenneth W. Harder, Colin J. D. Ross, Pieter R. Cullis,* and Anna K. Blakney*

Cite This: ACS Appl. Mater. Interfaces 2025, 17, 3097−3105

ABSTRACT: When formulating mRNA into lipid nanoparticles (LNP), various copy numbers of mRNA are encapsulated, leading to a distribution of mRNA loading levels within the LNPs. It is unclear whether the mRNA loading level affects the functional delivery of the message. Here we show that depending on the mRNA loading level, LNPs exhibit distinct mass densities and can be fractionated via ultracentrifugation. Upon fractionation, we investigated if mRNA loading levels influence LNP sizing, lipid composition, and morphology. We further conducted *in vitro* and *in vivo* functional delivery of mRNA and found that the LNP fraction with the highest mRNA loading levels was the least transfection competent.

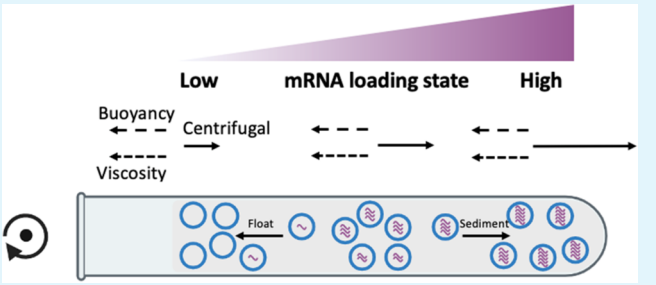

KEYWORDS: *lipid nanoparticles, mRNA, therapeutics, encapsulation, fractionation*

INTRODUCTION

Ribonucleic acid (RNA) nanomedicine has been clinically proven in recent years with the approval of small interfering RNA (siRNA) therapies such as Onpattro,[1] which treats transthyretin-induced amyloidosis (hATTR) and the Pfizer/BioNTech[2] and Moderna[3] mRNA vaccines against COVID-19, and most recently, the Moderna[4] mRNA vaccine against Respiratory Syncytial Virus. All four of these medicines use lipid nanoparticle (LNP) formulations to deliver the RNA. However, there are missing links between LNP structure and performance in RNA functional delivery, including how the mRNA copy number in LNPs impacts translation into the intended proteins.

The formulation of lipid nanoparticles is driven by the fusion of nanosized vesicles[5] in a random fashion. As a result, in the same batch of lipid nanoparticles, one LNP could contain n copies of mRNA with n = 0, 1, 2, 3, 4, *etc.*[6,7] As the final size of LNPs is largely dictated by the surface concentration of hydrophilic poly(ethylene glycol) (PEG) lipids to terminate the fusion induced by the conversion of ionizable lipids to the neutral state, the size of the LNP does not necessarily reflect the number of mRNA copies it contains. Thus, separation based on size is unlikely to reflect the mRNA loading level.

Alternatively, nucleotides and lipids possess distinct mass/buoyant densities. Single-stranded RNA has a density of ∼1.6 g/cm^3 (measured in potassium iodine gradient[8] and free mRNA was found to sediment during centrifugation[9]). The lipid species generally have a mass density in the range of 0.8−1.1 g/cm^3, depending on their chemical composition and molecular configuration. The empty LNPs (eLNPs) formed using the lipid compositions applied in Onpattro/Comirnaty/Spikevax were found to be lighter than the aqueous buffer (see below the literature update on using analytical ultracentrifugation (AUC) to measure LNPs). Thus, the mRNA−LNP formulation's mass density depends on the mRNA loading level. The LNPs with low mRNA loading will likely be less dense than the aqueous buffer (*e.g.*, phosphate-buffered saline (PBS) buffer has a density of ∼1.013 g/cm^3 at 25 °C[10]), while the highly loaded LNPs could be heavier. The density contrast between LNPs with various mRNA loading levels and their aqueous environment thus provides the basis for a centrifugation-based fractionation method.

A previous study used a centrifugation-based technique, called analytical ultracentrifugation (AUC)[11] to analyze LNPs. Henrickson et al.[11] measured the nucleotide drug (siRNA)

Received: November 17, 2024
Revised: December 21, 2024
Accepted: December 24, 2024
Published: December 31, 2024

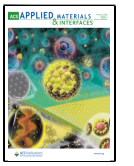

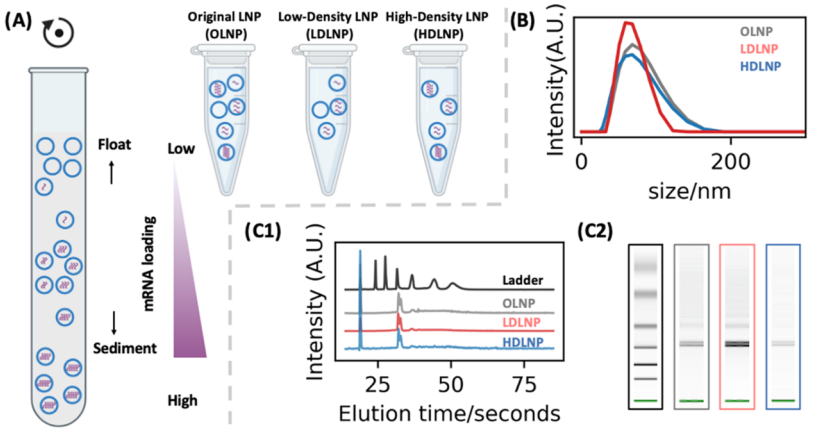

Figure 1. Centrifugal fractionation of LNPs based on their mRNA loading levels. (A) Schematic illustration of LNP fractionation via ultracentrifugation. Depending on the LNPs' density contrast with the aqueous system, two fractions (LDLNP and HDLNP) are generated from the fractionation process. Together with the original batch, three samples are compared throughout this paper; (B) particle size distribution by intensity measured with DLS; payload mRNA integrity by Bioanalyzer shown as electropherograms in (C1) and bands in (C2).

loading in LNPs with density-matching AUC. In the experiment, they tuned the density of the aqueous buffer by varying the fraction of heavy water and then measured the sedimentation coefficient of the LNP samples. They found that under certain buffer conditions, empty LNPs (eLNPs) float, LNPs with an N/P ratio of 6 (N/P ratio is the ratio between the positively charged nitrogen groups from the ionizable lipids and the negatively charged phosphate group from RNA) also float, while LNPs formulated at an N/P ratio of 1, thus higher RNA loading, sediment. Similar approaches were applied by Bepperling et al.[12] to estimate an average loading of five copies of mRNA in one LNP particle. Previously, our group (Leung et al.[13]) applied sucrose density gradient centrifugation to separate LNPs containing siRNA. Vaidya et al.[14] demonstrated the utilization of the same technique (sucrose gradient) to separate LNPs based on their mRNA loading level. Recently, Zhao et al.[15] have performed sedimentation velocity AUC on Pfizer/BioNTech mRNA LNPs and found the majority float in a centrifugal field, in agreement with the work from Calzolai[9] and co-workers.

Here we show the feasibility of fractionating LNPs with distinct mRNA loading levels by centrifugation in the original storage buffer. We use DLin-KC2-DMA (KC2)[16] as the ionizable lipid to formulate the model LNPs at a benchmark composition of KC2/distearoylphosphatidylcholine (DSPC)/cholesterol/PEG-DMG (50/10/38.5/1.5 mol %). Upon separation, we characterized the morphology of LNPs subpopulations with cryoEM. We further investigated the *in vitro* and *in vivo* functional delivery by fractionated LNP subpopulations.

RESULTS AND DISCUSSION

Centrifugal Fractionation of LNPs and the Integrity of LNP/mRNA. Under centrifugation, nanoparticles experience three major forces: centrifugal force, frictional force, and buoyant force. Balancing the three forces yields the so-called Svedberg equation,[17] describing nanoparticles' terminal velocity under a unit centrifugal field. For lipid nanoparticles from the same batch, we assume the constant size and shape (thus, constant volume v_{LNP}). We transform the Svedberg equation to show that the particle moving direction (or the sign of the sedimentation coefficient) depends on the density contrast between the particle and the buffer (for complete mathematical analysis, see the Supporting Information).

$$\frac{s_{LNPa}}{s_{LNPb}} \approx v_{LnP}\frac{\rho_{LNPa} - \rho_{sol}}{\rho_{LNPb} - \rho_{sol}} \quad (1)$$

LNPs' terminal velocity (magnitude and direction) in a centrifugal field largely depends on their mass density. (s: Svedberg coefficient; v_{LNP}: volume of LNPa/LNPb; ρ_{LNPa}, ρ_{LNPb}, ρ_{sol}: densities of LNPa, LNPb, and solvent, respectively.)

As shown in eq 1, for LNPa and LNPb, when one is heavier, while the other is lighter than the solvent, their moving direction diverges on centrifugation.

In brief, we rapidly mixed firefly luciferase mRNA (mFluc) and the lipid cocktail through a T junction at an N/P ratio of 6. The mixture was dialyzed overnight in PBS buffer to produce the final form of LNPs. We then centrifuged the LNPs at ~300 000 RCF for 2 h. Upon terminating the ultracentrifugation, we collected upper one-third and lower two-thirds by volume from the centrifuge tube and further refer the subpopulations as low-density LNPs (LDLNPs) and high-density LNPs (HDLNPs), respectively. The original batch is referred to as OLNP hereafter. Figure S1 depicts LNPs (labeled with DiD, thus appearing blue to provide visual inspection) before and after centrifugation. The workflow of the fractionation process is demonstrated schematically in Figure 1A. We validated the structural integrity of LNPs upon ultracentrifugation via DLS (Figure 1B, size distribution by intensity) and the RiboGreen assay to show that the subpopulations are within the size range of the original batch and no release of mRNA with encapsulation efficiency over 98% (Figure S2). As the RiboGreen assay does not characterize the integrity of mRNA, we evaluated the intactness of payload mRNA via capillary electrophoresis. No indication of mRNA degradation was found (Figure 1C). The percentage integrities of encapsulated mRNAs were found to be 91.7, 94.4, and 91.0% for OLNP, LDLNP, and HDLNP, respectively.

Characterization of Lipid Composition and N/P Ratio. To further characterize the properties of the fractionated LNPs, we quantified the cholesterol and mRNA concentration, respectively. The bar chart in Figure 2A uses the ratio of mRNA/lipid to characterize the mass of mRNA formulated in

https://doi.org/10.1021/acsami.4c20077
ACS Appl. Mater. Interfaces 2025, 17, 3097−3105

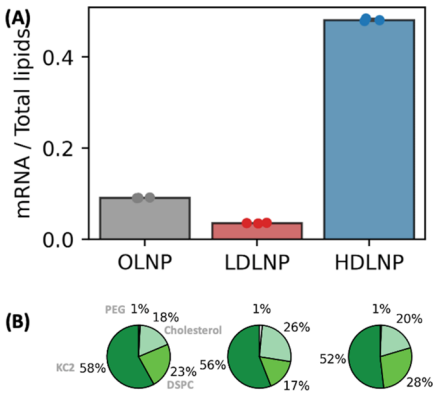

Figure 2. Validation of centrifugal fractionation, characterization of lipid composition, and calculation of N/P ratio. (A) Bar chart of RNA/total lipid ratio to represent the mRNA loading levels and validate the fractionation method; (B) pie charts showing lipid composition of OLNP, LDLNP, and HDLNP as characterized by ultrahigh-performance liquid chromatography−mass spectrometry (UHPLC-MS).

the subpopulation of LNPs containing unit mass of total lipids. The higher the ratio of mRNA/lipid, the higher the mRNA loading in that fraction.

The encapsulation of mRNA into LNP relies on self-assembly[18] events triggered primarily by the electrostatic attraction between nucleic acids and the ionizable lipids. We question whether the variation of mRNA loading could lead to significant variation in lipid compositions between fractions with different densities. To determine this, we performed UHPLC-MS; however, no significant difference between the original batch and the subpopulations (Figure 2B) was observed. This agrees with previous studies characterizing LNP lipid composition using SANS,[19] where it is shown that using different N/P ratios during formulation does not alter the final lipid composition. Combining the lipid composition and mRNA/lipid ratio, the actual N/P ratios are calculated to be 2.9, 7.5, and 0.5, for OLNP, LDLNP, and HDLNP, respectively.

LNP Morphology Depends on mRNA Loading Level. Currently, we lack an understanding of how the loading levels of mRNA influence the morphology of LNPs.[20] Previous work has suggested that the mRNA-loaded LNPs at neutral pH are coated with phospholipid mono-[21,22] or bilayers[23] with mRNA encapsulated within polar environments surrounded primarily by helper lipids that can form monolayers and bilayers such as DSPC and cholesterol.[24] This is consistent with the fact that the presence of helper lipids is essential for encapsulation.[1] The neutral form of the ionizable lipid has limited solubility in monolayer or bilayer lipid structures, as evidenced by phase separation into the hydrophobic "oil droplet" electron-dense core. The polar environments can frequently be visualized as "bleb" structures,[25−27] local aqueous compartments within the LNPs. It would be expected that the presence of larger numbers of mRNA within an LNP would lead to larger or more bleb structures. We therefore examined the LNP subpopulations using cryoEM (Figure 3A) and analyzed the images to investigate how LNPs' morphologies (size and anisotropy) depend on mRNA loading level.

In Figure 3A1, we show that the as-prepared LNPs are composed of spherical LNPs without blebs and nonspherical LNPs due to the formation of blebs.[26,27] LDLNPs, with relatively lower mRNA loading, the majority (∼70%) of LNPs is found without blebs, while the rest exhibit single small blebs; the particles from HDLNPs, when possessing blebs, however, exhibit larger blebs and occasionally multiple blebs docking on the same particle (Figure 3A2,A3). The composition of LNPs with various numbers of blebs is visualized as pie charts in Figure 3B.

To characterize the size and anisotropy of LNPs and the size of blebs, we measured the LNPs from the cryoEM images with FIJI. To reflect the anisotropy of LNPs, we measured both the polar diameter (the longest distance within the LNPs; denoted as X) and the equatorial diameter (denoted as Y) of LNPs. To

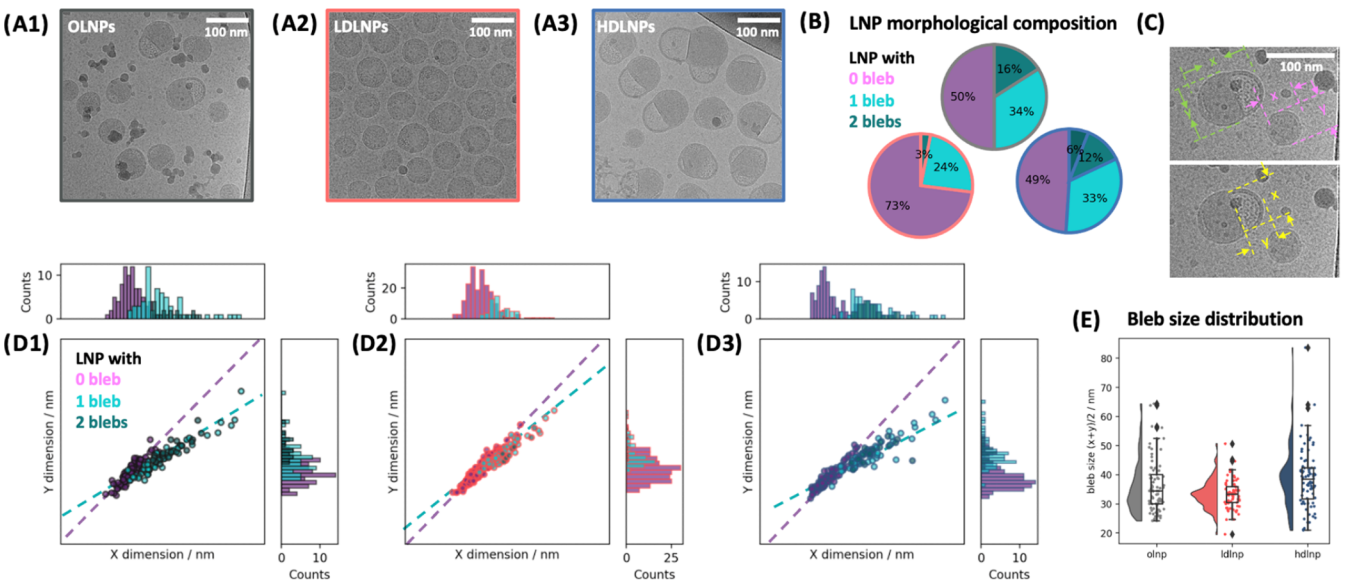

Figure 3. mRNA loading levels can influence the distribution of LNP morphology. (A1−A3) Representative cryoEM images of OLNP, LDLNP, and HDLNP (scale bar: 100 nm); (B) pie charts showing the composition of LNPs with various number of blebs; (C) schematic illustration of measuring LNPs and blebs with FIJI; (D1−D3) scatter plots mapping the dimension of LNPs and blebs (purple dots: LNPs without blebs; green dots: LNPs with blebs) (E) raincloud plot showing the size distribution of blebs.

https://doi.org/10.1021/acsami.4c20077
ACS Appl. Mater. Interfaces 2025, 17, 3097−3105

reflect the size of the blebs, we measured the width of the lipid−water interface (denoted as X) and the height of the blebs (denoted as Y). The measurement scheme is illustrated in Figure 3C.

In Figure 3D, we mapped the polar diameter X and the equatorial diameter Y of LNPs as scatter plots to display the absolute size of LNPs (the edge color of the marker is consistent with the color scheme used for OLNP/LDLNP/HDLNP while the face color choice reflects the number of blebs, purple for particles without blebs, green in various shades for particles with blebs, in consistency with Figure 3B). The slope of the linear trend line by fitting X and Y of LNPs serves as an indicator of the anisotropy of LNPs. Dimensions in X and Y were also projected as histograms to indicate the size distribution of LNPs. First, we point out the correlation between the percentage of particles with blebs and the mRNA loading level (50, 27, and 51% for OLNP, LDLNP, and HDLNP, respectively). Second, we note that particles without blebs are anisotropic (isotropy being 0.98, 1.00, and 1.02) and share very similar sizes (52.1, 55.1, and 49.1 nm) in all three types of LNPs; for particles with blebs, the size (69.6, 68.7, and 74.6 nm) and isotropy (1.19, 1.08, and 1.23) depend on mRNA loading levels. (The overall size distribution as measured by cryoEM is visualized in Figure S3.) Third, we found that the mRNA loading level also influences the size distribution of bleb size. The average sizes of blebs from OLNP/LDLNP/HDLNP are 37.1, 33.8, and 42.0 nm (bleb size distribution shown in Figure 3E). Finally, the observation of multibleb LNPs motivated us to calculate the average number of blebs on the same LNP and found the value to be 1.23, 1.11, and 1.48 for OLNP, LDLNP, and HDLNP, respectively.

Taken together, we conclude that the mRNA loading level can influence the morphology of the particles with blebs but not the particles without blebs. Higher loading level leads to larger LNPs with higher anisotropy, larger blebs, and/or more multibleb LNPs. The statistics from cryoEM, together with the effective N/P ratio, are summarized in Table 1 to present the reader with a quantitative viewpoint. More representative cryoEM images can be found in Figure S4.

Table 1. Quantification of LNP Morphologies Based on CryoEM Images

		OLNP	LDLNP	HDLNP
composition (LNP with *vs* without blebs)		50:50	73:27	49:51
particles without blebs	size/nm	52.1	55.1	49.1
	isotropy	0.98	1.00	1.02
particles with blebs	size/nm	69.6	68.7	74.6
	isotropy	1.19	1.08	1.23
	bleb size/nm	37.1	33.8	42.0
average number of blebs per particle (with blebs)		1.23	1.11	1.48
	N/P ratio	2.9	7.5	0.5

***In Vitro* mRNA Delivery with OLNP, LDLNP, and HDLNP.** We studied the cellular interactions of OLNP/LDLNP/HDLNPs using mRNA encoding enhanced green fluorescence protein with covalently conjugated cyanine 5 (Cy5-mEGFP) as a reporter gene. We incubated the Cy5-mEGFP-loaded OLNP/LDLNP/HDLNP with HEK293 cells and inspected both Cy5 and EGFP signals with confocal laser scanning microscopy (CLSM). As the dose of Cy5-mEGFP is controlled, the Cy5 signal reports the cellular uptake of mRNA/LNPs while the EGFP signal reports the actual expression, namely, the functional delivery of the mRNA payload.

In Figure 4A, we show that while the level of cellular uptake of mRNA (indicated by the Cy5 channel) is comparable across three types of LNPs, the level of mEGFP expression varies. OLNP and LDLNPs express significantly more green fluorescence protein (GFP) than HDLNP. Semiquantification was further performed by line analysis of intensity with FIJI and plotted on top of the GFP and Cy5 channels. This result was reproduced with Huh7 cells (Figure S5). We also segmented each cell and quantified the mean fluorescent intensities, as shown in Figure S6. We hypothesize that this disparity between cell uptake and functional delivery can be attributed to particles' ability to escape from the endolysosomal systems. Thus, we studied the colocalization between LNP and late endosome. We labeled the late endosome with Rab7a fused with RFP before incubating with DiD-labeled LNPs. The visual inspection from Figure 4B indicates a significantly higher degree of colocalization between RFP/Rab7a and DiD/LNP in the case of HDLNPs, in comparison to OLNP/LDLNP. The colocalization analysis was performed, and we found that the Pearson's coefficient for HDLNP is ∼0.75, while the values are around 0.35 for either OLNP or LDLNP (Figure S7).

***In Vivo* mRNA Delivery with OLNP, LDLNP, and HDLNP.** As *in vitro* results have been repeatedly shown to be poorly predictive of *in vivo* performance,[28,29] we decided to test OLNP, LDLNP, and HDLNP in mice. We are trying to address two key research questions. Does the mRNA loading level in LNPs influence how well (potency) and where (biodistribution) the mRNA payloads are being translated *in vivo*? We applied albino B6 (B6(Cg)-*Tyr*$^{c\text{-}2J}$/J) mice as the mouse model for our animal work as the original C57BL/6J strain has been widely used for nanomedicine study, while the albino substrain offers higher signal-noise ratio when performing bioluminescence experiments. In brief, for each LNP formulation, we injected albino B6 mice (n = 4) through their tail vein at the dose of 0.3 mg mRNA/kg of mouse weight. Three hours post-injection, the mice were dosed with D-luciferin through intraperitoneal route and then anesthetized for *in vivo* imaging. Two major organs that are relevant to "Onpattro-like" LNP formulations, liver and spleen, were harvested after euthanizing the mice for *ex vivo* imaging.

We found, in accordance with the *in vitro* assay, that HDLNPs are the least potent formulation in the functional delivery of mRNA *in vivo*. The expression of the mFluc payload is 20-fold less by HDLNPs than those encapsulated in OLNP/LDLNP (Figure 5B). The same trend is maintained for liver and spleen luminescence (Figure 5C). For a visual presentation of liver−spleen tropism, we project the liver radiance against spleen radiance by making a scatter plot in Figure 5D. No significant alteration of tissue distribution can be observed. While the HDLNPs express 20-fold less than OLNP/LDLNP, the bioluminescence signal is still 1000-fold above the saline control. The LDLNPs produce ∼50% more luminescence than OLNPs. The trend is likely due to the absence of the less potent HDLNP fraction in LDLNP from OLNP but could also be attributed to the enrichment of empty LNPs, whose role in mRNA therapeutic delivery is largely unknown.

https://doi.org/10.1021/acsami.4c20077
ACS Appl. Mater. Interfaces 2025, 17, 3097−3105

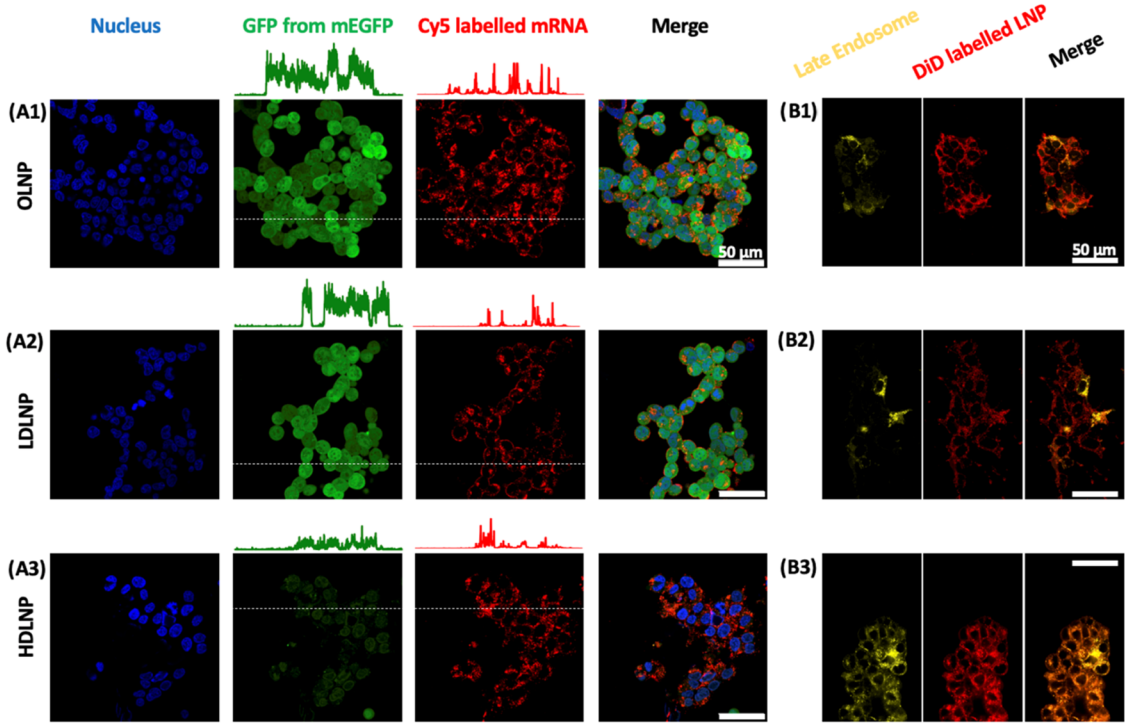

Figure 4. Cellular uptake and functional delivery of mRNA with OLNP, LDLNP, and HDLNP. (A) CLSM images of OLNP, LDLNP, and HDLNP ((A1), (A2), and (A3), respectively) delivering Cy5-labeled mEGFP into HEK293 cells (scale bar: 50 μm); (B1−B3) CLSM study on the colocalization between LNP colocalization and Rab7a, representing late endosomes (scale bar: 50 μm).

CONCLUSIONS

We have shown that ultracentrifugation is an effective technique to fractionate LNPs based on their mRNA loading level without disturbing the integrity of neither LNP nor mRNA. The mRNA loading level has an influence on LNPs' overall morphology. As shown above by the cryoEM images, the LNP fraction with a relatively lower mRNA loading level displays smaller and fewer blebs, while the LNP fraction with high mRNA loading exhibits larger and multibleb constructs. Thus, taken together, the distribution of the mRNA loading level within the same batch of LNPs translates to a distribution of N/P ratios. Although intuitive thought leads one to prefer the LNP fraction with high mRNA loading, our *in vitro* and *in vivo* experiments revealed that they are the least potent population in the formulation, likely due to their deviation from the optimal N/P ratio. Moreover, we have shown that the mRNA loading level mainly alters LNPs' potency but not the biodistribution of the proteins expressed by the mRNA payload.

However, we must point out several weaknesses and unanswered questions of this work. First, this centrifugal fractionation has low resolution in separating, as it is solely based on the density contrast of LNPs against the aqueous buffer. The low resolution is mainly due to the requirement of density contrast with the aqueous buffer and also partly due to nanoparticles' fast diffusion. One could add more resolution to such separation by building a sucrose gradient as recently shown.[14] However, the added viscosity requires a higher centrifugal field and/or extended centrifugation time, not to mention the possible unwanted sucrose-lipid interactions. These factors might alter the identities of LNPs. Furthermore, what is the role of empty LNPs? The fractionation process presented herein could not remove eLNPs from either of the subpopulations. Thus, the role of empty LNPs in the functional delivery of mRNA therapeutics is still unclear. We hope to share our insights into the role of eLNPs in another work in the future. Finally, although we have shown (Figure 1) that the fractionation does not damage neither LNP nor mRNA, this does not necessarily indicate no alteration on the molecular level. Does the mechanical stress, especially the centrifugal force and the frictional force, alter the LNPs by rearranging lipids or a phase redistribution? This would require a meticulous study using small-angle X-ray scattering and small-angle neutron scattering (with selectively deuterated lipids).

To conclude this work, we point out several promising directions to optimize LNP formulations. Since the mRNA loading level could impact LNPs' potency, there is substantial interest in developing better fractionation with higher granularity and understanding if there is and what is the optimal copy number of mRNA (or N/P ratio) inside one LNP. With the understanding of the ideal N/P ratio, we should design LNP formulating strategies to encapsulate mRNA in the most optimal subpopulation of the intrinsically heterogeneous LNPs. Most ideally, one should aim to develop formulation strategies to generate homogeneous LNPs with the optimal mRNA loading level.

METHODS

Materials. The lipids DSPC and PEG-DMG-2000 were purchased from Avanti Polar Lipids. The ionizable lipids DLin-KC2-DMA were purchased from Dr. Marco Ciufolini. Cholesterol was purchased from Sigma-Aldrich. Dulbecco's modified Eagle's medium (DMEM) and fetal bovine serum (FBS) were purchased from Thermo Fisher Scientific. All other chemicals were purchased from Sigma-Aldrich unless otherwise stated. Firefly luciferase mRNA (mFluc) was purchased from NanoVation Therapeutics, Inc. by S.L. and A.K.B.

https://doi.org/10.1021/acsami.4c20077
ACS Appl. Mater. Interfaces 2025, 17, 3097−3105

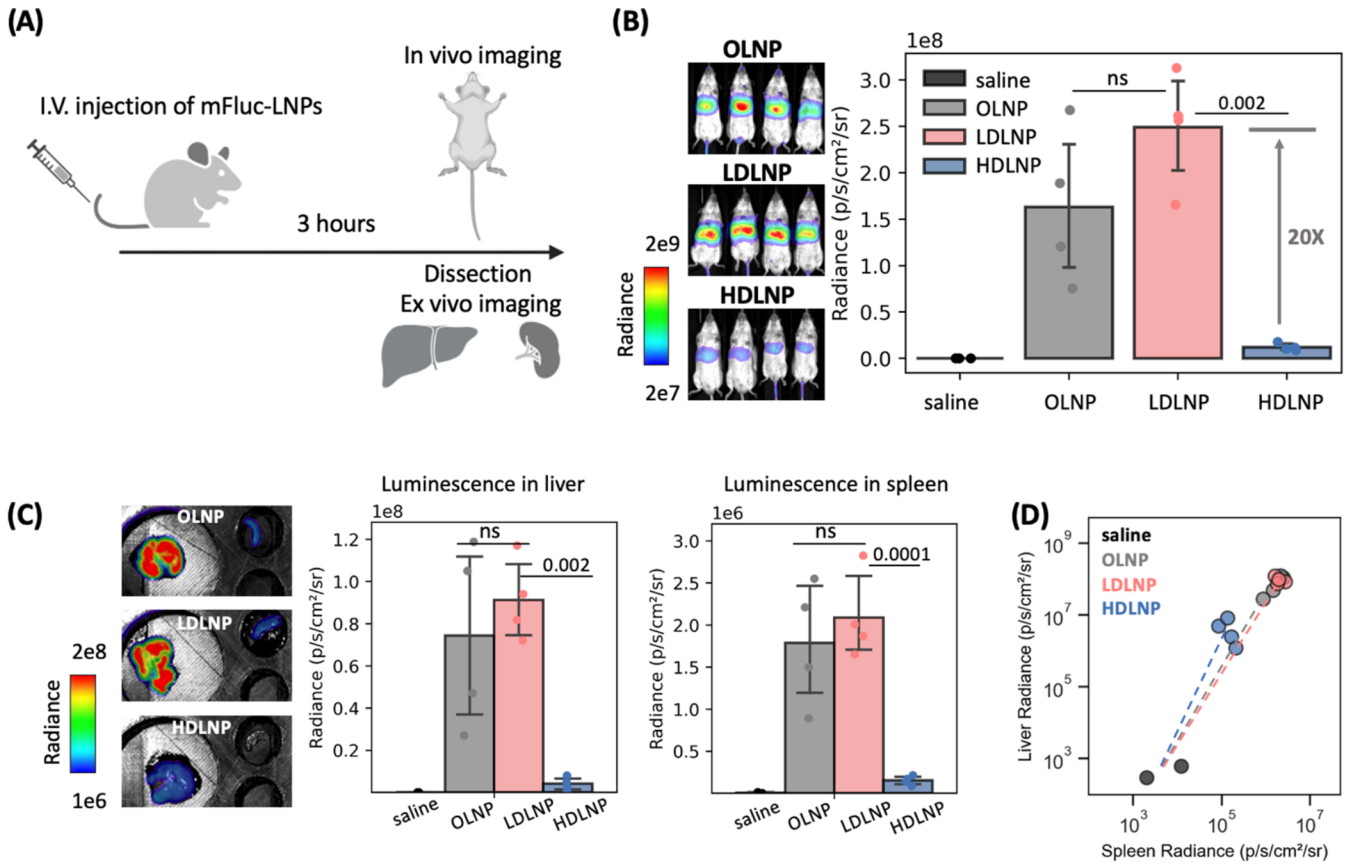

Figure 5. *In vivo* functional delivery of mFluc. (A) Schematic illustration of the animal study; (B) *in vivo* bioluminescence images of mice at 3 h after IV injection at mFluc dosage of 0.3 mg/kg (n = 4) and bar chart showing whole-body bioluminescence quantification from IVIS imaging. Data are presented as the mean ± standard deviation (SD) (n = 4). (C) Representative *ex vivo* bioluminescence images of extracted livers and spleens from mice dosed with OLNP/LDLNP/HDLNP (top to bottom) and bar chart showing bioluminescence of extracted livers and spleens. Data are presented as the mean ± SD (n = 4). (D) Scatter plot by projecting *ex vivo* liver radiance readout against spleen readout to indicate tissue tropism.

Cy5-mEGFP was provided by Dr. Andrew J. Varley (RNA and Formulation Core of UBC).

LNP Formulation and Characterization. All LNPs were formulated by first dissolving lipids (ionizable lipid, DSPC, cholesterol, PEG-DMG-2000) into ethanol to a final concentration of 10 mM and at a molar ratio of 50/10/38.5/1.5%, respectively. Then, the lipid−ethanol mixture was rapidly mixed with mRNA in aqueous buffer (25 mM sodium acetate at pH 4) at an amine-to-phosphate ratio of 6. The rapid mixing was achieved using a T junction at a 1:3 ethanol/water volume ratio and a total flow rate of 20 mL/min. The resulting mixture was dialyzed overnight against >500-fold volume of PBS at pH 7.4. Upon dialysis, the mixture was then sterile filtered through Supor membrane syringe filter (Pall Corporation, Mississauga, ON, Canada) at the size cutoff of 0.2 μm and then concentrated via ultrafiltration using Amicon ultra-centrifugation units with 100k molecular weight cutoff (EMD Millipore Corporation, Billerica, MA). Total lipid content was determined by extrapolation using the Cholesterol E Kit (Wako Diagnostics, Mountain View, CA). Particle size was measured via dynamic light scattering using the Malvern Zetasizer Nano ZS.

Bioanalyzer. mRNA extracted from LNPs was prepared according to the Agilent RNA 6000 Nano kit guide and run on the Agilent Bioanalyzer 21000 using the mRNA Nano assay protocol. Percentage of intact mRNA was determined by obtaining the area under the curve of the mFluc peak on the electrogram.

Cryo-TEM. The freshly prepared LNPs were concentrated to ∼20 mg/mL of total lipid concentration, added to glow-discharged copper grids (3−5 μL), and plunge-frozen using an FEI Mark IV Vitrobot (FEI, Hillsboro) to generate vitreous ice. Grids were moved into a Gatan 70° cryotilt transfer system preequilibrated to at least −180 °C and then inserted into the microscope. An FEI LaB6 G2 TEM (FEI, Hillsboro, OR) operating at 200 kV under low-dose conditions was used to image all samples with an FEI Eagle 4k CCD camera. All samples were imaged at 55 000× magnification with a nominal underfocus of 1−2 μm to enhance contrast. All sample preparation and imaging were performed at the UBC Bioimaging Facility (Vancouver, BC).

Liquid Chromatography−Mass Spectrometry (LC-MS) Analysis. The LNP formulation was further diluted to a 10 μM concentration in a solution of 70% acetonitrile and 30% isopropyl alcohol before LC-MS analysis. The analysis was conducted using an Impact II high-resolution spectrometer (Bruker Daltonics, Bremen, Germany) coupled with an Elute UHPLC system (Bruker Daltonics). Compounds were separated using an Acquity CSH C18 column (130 Å, 1.7 μm, 100 × 2.1 mm^2) with a CSH C18 VanGuard FIT Cartridge (1.7 μm, 2.1 × 5 mm^2) (Waters, Milford, MA) and a multigradient method. The analysis utilized mobile phase A (acetonitrile/water 60:40 v/v) and mobile phase B (isopropanol/acetonitrile 90:10 v/v), both containing 0.1% formic acid and 10 mM ammonium formate. The gradient profile was as follows: 0 min, 15% B; 0−2 min, 30% B; 2−2.5 min, 50% B; 2.5−12 min, 80% B; 12−12.5 min, 99% B; 12.5−13.5 min, 99% B; 13.5−13.7 min, 15% B; 13.7−17 min, 15% B. The column temperature was set at 65 °C, flow rate at 0.5 mL/min, injection volume at 1 μL, and autosampler at 4 °C. Data-dependent acquisitions were acquired in positive (ESI+) ionization mode. The settings were as follows: capillary voltage, 4500 V; nebulizer gas pressure, 2.0 bar; dry gas flow, 9 L/min; dry gas temperature, 220 °C; mass scan range, 100−1700 m/z; spectra acquisition rate, 3 Hz; and cycle time, 0.7 s.

https://doi.org/10.1021/acsami.4c20077
ACS Appl. Mater. Interfaces 2025, 17, 3097−3105

Cell Culture and Treatments. A human hepatocarcinoma cell line (Huh7) was cultured and maintained in DMEM media supplemented with 10% FBS, at 37 °C under 5% CO_2. For transfection with LNPs, ∼10 000 cells per well were seeded into 96-well microplates for 24 h before treating with the LNP containing mFluc at mRNA dosage from 0 to 0.3 μg/mL. Upon 24 h of incubation, the medium was removed, and cells were lysed with 100 μL of Glo Lysis buffer (Promega, Madison, WI). The lysates were mixed at a 1:1 ratio with luciferase substrate (Promega, Madison, WI) and luminescence was quantified using a Spark Multimode Microplate reader (Tecan, Zürich, Switzerland). Luminescence readings were then normalized to the total protein content per well and determined using the Pierce BCA Protein Assay Kit (Thermo Fisher Scientific, Rockford, IL), and transfection was calculated by normalizing to the luminescence values for untreated cells.

Animal Studies. All animal protocols were approved by the Canadian Animal Care Committee and conducted in accordance with the relevant UBC guidelines and regulations. Mice were maintained on a regular 12 h light/12 h dark cycle in a modified barrier animal facility at UBC. C57BL/6J-TyrC2J mice aged between 8 and 12 weeks were used throughout. The mice were individually weighed and imaged prior to tail vein intravenous (i.v.) injection of LNP containing mFluc at an mRNA dose of 0.3 mg/kg of mouse weight. At 3 h post-injection, mice were administered D-luciferin substrate solution (150 mg/kg of mouse weight) intraperitoneally for an incubation period of 10 min before *in vivo* bioluminescence imaging. Mice belonging to the same dosing groups (n = 3/4) were anesthetized with 3% isoflurane and placed on the imaging platform in a supine position with the inhalation of 3% isoflurane via nose cones. The mice were imaged 10 min post administration of D-luciferin and imaged on the LagoX IVIS Spectrum *In Vivo* Imaging System, with an exposure time of 10 s. Quantification of bioluminescence was performed by measuring the radiance (photons/s/cm^2/steradian) from the regions of interest (abdominal region) using the Aura Imaging Software (Spectral Instruments Imaging).

Immediately following the IVIS imaging (3 h post-injection), the mice were euthanized, and livers and spleens were collected and imaged *ex vivo*. Bioluminescence values were quantified by the radiance (photons/s/cm^2/steradian) for each tissue using the LagoX IVIS Spectrum *In Vivo* Imaging System.

Statistical Analysis. All data were reported as the mean ± the standard error of the mean (SEM). Comparisons were made between distinct groups by analyzing with one-way analysis of variance (ANOVA). Statistical significance, or P values, were reported directly on the figure. P values below 0.5 were considered nonsignificant (ns). Data analysis and visualization were performed by python scripting.

■ ASSOCIATED CONTENT

Supporting Information

The Supporting Information is available free of charge at https://pubs.acs.org/doi/10.1021/acsami.4c20077.

Mathematical deduction of eq 1; photos of DiD-labeled LNPs before and after ultracentrifugation (Figure S1); RiboGreen assay results show encapsulation efficiency (Figure S2); LNP size distribution by cryoEM (Figure S3); other representative cryoEM images (Figure S4); cellular uptake and functional delivery of mRNA in Huh7 cells (Figure S5); quantification of CLSM images (Figure S6); and colocalization analysis shown as Pearson's coefficient (Figure S7) (PDF)

■ AUTHOR INFORMATION

Corresponding Authors

Pieter R. Cullis − *Department of Biochemistry and Molecular Biology, University of British Columbia, Vancouver, British Columbia V6T 1Z3, Canada;* orcid.org/0000-0001-9586-2508; Email: pieterc@mail.ubc.ca

Anna K. Blakney − *Michael Smith Laboratories, University of British Columbia, Vancouver, British Columbia V6T 1Z4, Canada; School of Biomedical Engineering, University of British Columbia, Vancouver, British Columbia V6T 2B9, Canada;* orcid.org/0000-0002-5812-9689; Email: anna.blakney@msl.ubc.ca

Authors

Suiyang Liao − *Department of Biochemistry and Molecular Biology, University of British Columbia, Vancouver, British Columbia V6T 1Z3, Canada; Michael Smith Laboratories, University of British Columbia, Vancouver, British Columbia V6T 1Z4, Canada; School of Biomedical Engineering, University of British Columbia, Vancouver, British Columbia V6T 2B9, Canada*

Shuangyu Wang − *Department of Biochemistry and Molecular Biology, University of British Columbia, Vancouver, British Columbia V6T 1Z3, Canada*

Abishek Wadhwa − *Department of Microbiology and Immunology, University of British Columbia, Vancouver, British Columbia V6T 1Z3, Canada; Life Sciences Institute, University of British Columbia, Vancouver, British Columbia V6T 1Z3, Canada*

Alexandra Birkenshaw − *Faculty of Pharmaceutical Sciences, University of British Columbia, Vancouver, British Columbia V6T 1Z3, Canada*

Kevin Fox − *Department of Biochemistry and Molecular Biology, University of British Columbia, Vancouver, British Columbia V6T 1Z3, Canada; Faculty of Pharmaceutical Sciences, University of British Columbia, Vancouver, British Columbia V6T 1Z3, Canada*

Miffy Hok Yan Cheng − *Department of Biochemistry and Molecular Biology, University of British Columbia, Vancouver, British Columbia V6T 1Z3, Canada;* orcid.org/0000-0002-0261-4642

Irafasha C. Casmil − *Michael Smith Laboratories, University of British Columbia, Vancouver, British Columbia V6T 1Z4, Canada; School of Biomedical Engineering, University of British Columbia, Vancouver, British Columbia V6T 2B9, Canada;* orcid.org/0000-0003-1890-7930

Armando Alcazar Magana − *Michael Smith Laboratories, University of British Columbia, Vancouver, British Columbia V6T 1Z4, Canada; Life Sciences Institute, University of British Columbia, Vancouver, British Columbia V6T 1Z3, Canada*

Nuthan Vikas Bathula − *Michael Smith Laboratories, University of British Columbia, Vancouver, British Columbia V6T 1Z4, Canada; School of Biomedical Engineering, University of British Columbia, Vancouver, British Columbia V6T 2B9, Canada*

Chia Hao Ho − *Michael Smith Laboratories, University of British Columbia, Vancouver, British Columbia V6T 1Z4, Canada;* orcid.org/0000-0003-3670-2680

Jin-Yu Cheng − *Department of Biochemistry and Molecular Biology, University of British Columbia, Vancouver, British Columbia V6T 1Z3, Canada*

Leonard J. Foster − *Department of Biochemistry and Molecular Biology, University of British Columbia, Vancouver, British Columbia V6T 1Z3, Canada; Michael Smith Laboratories, University of British Columbia, Vancouver, British Columbia V6T 1Z4, Canada; Life*

https://doi.org/10.1021/acsami.4c20077
ACS Appl. Mater. Interfaces 2025, 17, 3097−3105

Sciences Institute, University of British Columbia, Vancouver, British Columbia V6T 1Z3, Canada; orcid.org/0000-0001-8551-4817

Kenneth W. Harder − *Department of Microbiology and Immunology, University of British Columbia, Vancouver, British Columbia V6T 1Z3, Canada; Life Sciences Institute, University of British Columbia, Vancouver, British Columbia V6T 1Z3, Canada*

Colin J. D. Ross − *Faculty of Pharmaceutical Sciences, University of British Columbia, Vancouver, British Columbia V6T 1Z3, Canada*

Complete contact information is available at: https://pubs.acs.org/10.1021/acsami.4c20077

Author Contributions

The manuscript was written through contributions of all authors. All authors have given approval to the final version of the manuscript.

Funding

This work was supported by a NanoMedicine Innovative Network (NMIN) Grand Challenge grant to A.K.B., P.R.C., K.W.H., C.J.D.R., and L.J.F.; NMIN Graduate Award—Doctoral to ICC; MSFHR Scholar Award and Tier II Canada Research Chair to A.K.B.; NMIN Graduate Award—Doctoral and the UBC Four Year Doctoral Fellowship (4YF) Award to A.W.

Notes

The authors declare no competing financial interest.

REFERENCES

(1) Akinc, A.; Maier, M. A.; Manoharan, M.; Fitzgerald, K.; Jayaraman, M.; Barros, S.; Ansell, S.; Du, X.; Hope, M. J.; Madden, T. D.; Mui, B. L.; Semple, S. C.; Tam, Y. K.; Ciufolini, M.; Witzigmann, D.; Kulkarni, J. A.; van der Meel, R.; Cullis, P. R. The Onpattro Story and the Clinical Translation of Nanomedicines Containing Nucleic Acid-Based Drugs. *Nat. Nanotechnol.* **2019**, *14* (12), 1084−1087.

(2) Polack, F. P.; Thomas, S. J.; Kitchin, N.; Absalon, J.; Gurtman, A.; Lockhart, S.; Perez, J. L.; Pérez Marc, G.; Moreira, E. D.; Zerbini, C.; Bailey, R.; Swanson, K. A.; Roychoudhury, S.; Koury, K.; Li, P.; Kalina, W. V.; Cooper, D.; Frenck, R. W.; Hammitt, L. L.; Türeci, Ö.; Nell, H.; Schaefer, A.; Ünal, S.; Tresnan, D. B.; Mather, S.; Dormitzer, P. R.; Şahin, U.; Jansen, K. U.; Gruber, W. C. Safety and Efficacy of the BNT162b2 mRNA Covid-19 Vaccine. *N. Engl. J. Med.* **2020**, *383* (27), 2603−2615.

(3) Baden, L. R.; El Sahly, H. M.; Essink, B.; Kotloff, K.; Frey, S.; Novak, R.; Diemert, D.; Spector, S. A.; Rouphael, N.; Creech, C. B.; McGettigan, J.; Khetan, S.; Segall, N.; Solis, J.; Brosz, A.; Fierro, C.; Schwartz, H.; Neuzil, K.; Corey, L.; Gilbert, P.; Janes, H.; Follmann, D.; Marovich, M.; Mascola, J.; Polakowski, L.; Ledgerwood, J.; Graham, B. S.; Bennett, H.; Pajon, R.; Knightly, C.; Leav, B.; Deng, W.; Zhou, H.; Han, S.; Ivarsson, M.; Miller, J.; Zaks, T. Efficacy and Safety of the mRNA-1273 SARS-CoV-2 Vaccine. *N. Engl. J. Med.* **2021**, *384* (5), 403−416.

(4) Wilson, E.; Goswami, J.; Baqui, A. H.; Doreski, P. A.; Perez-Marc, G.; Zaman, K.; Monroy, J.; Duncan, C. J. A.; Ujiie, M.; Rämet, M.; Pérez-Breva, L.; Falsey, A. R.; Walsh, E. E.; Dhar, R.; Wilson, L.; Du, J.; Ghaswalla, P.; Kapoor, A.; Lan, L.; Mehta, S.; Mithani, R.; Panozzo, C. A.; Simorellis, A. K.; Kuter, B. J.; Schödel, F.; Huang, W.; Reuter, C.; Slobod, K.; Stoszek, S. K.; Shaw, C. A.; Miller, J. M.; Das, R.; Chen, G. L. Efficacy and Safety of an mRNA-Based RSV PreF Vaccine in Older Adults. *N. Engl. J. Med.* **2023**, *389* (24), 2233−2244.

(5) Kulkarni, J. A.; Witzigmann, D.; Leung, J.; van der Meel, R.; Zaifman, J.; Darjuan, M. M.; Grisch-Chan, H. M.; Thöny, B.; Tam, Y. Y. C.; Cullis, P. R. Fusion-Dependent Formation of Lipid Nanoparticles Containing Macromolecular Payloads. *Nanoscale* **2019**, *11* (18), 9023−9031.

(6) Li, S.; Hu, Y.; Lin, J.; Schneiderman, Z.; Shao, F.; Wei, L.; Li, A.; Hsieh, K.; Kokkoli, E.; Curk, T.; Mao, H.-Q.; Wang, T.-H. Single-Particle Spectroscopic Chromatography Reveals Heterogeneous RNA Loading and Size Correlations in Lipid Nanoparticles. *ACS Nano* **2024**, *18*, 15729.

(7) Li, S.; Hu, Y.; Li, A.; Lin, J.; Hsieh, K.; Schneiderman, Z.; Zhang, P.; Zhu, Y.; Qiu, C.; Kokkoli, E.; Wang, T.-H.; Mao, H.-Q. Payload Distribution and Capacity of mRNA Lipid Nanoparticles. *Nat. Commun.* **2022**, *13* (1), No. 5561.

(8) De Kloet, S. R.; Andrean, B. A. G. Buoyant Density Gradient Centrifugation of RNA and DNA in Alkali Iodide Solutions. *Biochim. Biophys. Acta, Nucleic Acids Protein Synth.* **1971**, *247* (4), 519−527.

(9) Guerrini, G.; Mehn, D.; Scaccabarozzi, D.; Gioria, S.; Calzolai, L. Analytical Ultracentrifugation to Assess the Quality of LNP-mRNA Therapeutics. *Int. J. Mol. Sci.* **2024**, *25* (11), No. 5718.

(10) Schiel, J. E.; Hage, D. S. Density Measurements of Potassium Phosphate Buffer from 4 to 45 °C. *Talanta* **2005**, *65* (2), 495−500.

(11) Henrickson, A.; Kulkarni, J. A.; Zaifman, J.; Gorbet, G. E.; Cullis, P. R.; Demeler, B. Density Matching Multi-Wavelength Analytical Ultracentrifugation to Measure Drug Loading of Lipid Nanoparticle Formulations. *ACS Nano* **2021**, *15*, 5068.

(12) Bepperling, A.; Richter, G. Determination of mRNA Copy Number in Degradable Lipid Nanoparticles via Density Contrast Analytical Ultracentrifugation. *Eur. Biophys J.* **2023**, *52*, 393.

(13) Leung, A. K. K.; Hafez, I. M.; Baoukina, S.; Belliveau, N. M.; Zhigaltsev, I. V.; Afshinmanesh, E.; Tieleman, D. P.; Hansen, C. L.; Hope, M. J.; Cullis, P. R. Lipid Nanoparticles Containing siRNA Synthesized by Microfluidic Mixing Exhibit an Electron-Dense Nanostructured Core. *J. Phys. Chem. C* **2012**, *116* (34), 18440−18450.

(14) Vaidya, A.; Parande, D.; Khadse, N.; Vargas-Montoya, N.; Agarwal, V.; Ortiz, C.; Ellis, G.; Kaushal, N.; Sarode, A.; Karve, S.; DeRosa, F. Analytical Characterization of Heterogeneities in mRNA-Lipid Nanoparticles Using Sucrose Density Gradient Ultracentrifugation. *Anal. Chem.* **2024**, *96*, 5570.

(15) Zhao, H.; Sousa, A. A.; Schuck, P. Flotation Coefficient Distributions of Lipid Nanoparticles by Sedimentation Velocity Analytical Ultracentrifugation. *ACS Nano* **2024**, *18*, 18663.

(16) Semple, S. C.; Akinc, A.; Chen, J.; Sandhu, A. P.; Mui, B. L.; Cho, C. K.; Sah, D. W. Y.; Stebbing, D.; Crosley, E. J.; Yaworski, E.; Hafez, I. M.; Dorkin, J. R.; Qin, J.; Lam, K.; Rajeev, K. G.; Wong, K. F.; Jeffs, L. B.; Nechev, L.; Eisenhardt, M. L.; Jayaraman, M.; Kazem, M.; Maier, M. A.; Srinivasulu, M.; Weinstein, M. J.; Chen, Q.; Alvarez, R.; Barros, S. A.; De, S.; Klimuk, S. K.; Borland, T.; Kosovrasti, V.; Cantley, W. L.; Tam, Y. K.; Manoharan, M.; Ciufolini, M. A.; Tracy, M. A.; de Fougerolles, A.; MacLachlan, I.; Cullis, P. R.; Madden, T. D.; Hope, M. J. Rational Design of Cationic Lipids for siRNA Delivery. *Nat. Biotechnol.* **2010**, *28* (2), 172−176.

(17) Svedberg, T.; Rinde, H. The Ultra-centrifuge, a New Instrument for the Determination of Size and Distribution of Size of Particle In Amicroscopic Colloids. *J. Am. Chem. Soc.* **1924**, *46* (12), 2677−2693.

(18) Kim, J.; Eygeris, Y.; Gupta, M.; Sahay, G. Self-Assembled mRNA Vaccines. *Adv. Drug Delivery Rev.* **2021**, *170*, 83.

(19) Gilbert, J.; Sebastiani, F.; Arteta, M. Y.; Terry, A.; Fornell, A.; Russell, R.; Mahmoudi, N.; Nylander, T. Evolution of the Structure of Lipid Nanoparticles for Nucleic Acid Delivery: From *in Situ* Studies of Formulation to Colloidal Stability. *J. Colloid Interface Sci.* **2024**, *660*, 66−76.

(20) Szebeni, J.; Kiss, B.; Bozó, T.; Turjeman, K.; Levi-Kalisman, Y.; Barenholz, Y.; Kellermayer, M. Insights into the Structure of Comirnaty Covid-19 Vaccine: A Theory on Soft, Partially Bilayer-Covered Nanoparticles with Hydrogen Bond-Stabilized mRNA−Lipid Complexes. *ACS Nano* **2023**, *17* (14), 13147−13157.

(21) Forchette, L.; Sebastian, W.; Liu, T. A Comprehensive Review of COVID-19 Virology, Vaccines, Variants, and Therapeutics. *Curr. Med. Sci.* **2021**, *41* (6), 1037−1051.

(22) Heinz, F. X.; Stiasny, K. Distinguishing Features of Current COVID-19 Vaccines: Knowns and Unknowns of Antigen Presentation and Modes of Action. *npj Vaccines* **2021**, *6* (1), No. 104.
(23) Buschmann, M. D.; Carrasco, M. J.; Alishetty, S.; Paige, M.; Alameh, M. G.; Weissman, D. Nanomaterial Delivery Systems for mRNA Vaccines. *Vaccines* **2021**, *9* (1), No. 65.
(24) Tenchov, R.; Bird, R.; Curtze, A. E.; Zhou, Q. Lipid Nanoparticles—From Liposomes to mRNA Vaccine Delivery, a Landscape of Research Diversity and Advancement. *ACS Nano* **2021**, *15* (11), 16982−17015.
(25) Kloczewiak, M.; Banks, J. M.; Jin, L.; Brader, M. L. A Biopharmaceutical Perspective on Higher-Order Structure and Thermal Stability of mRNA Vaccines. *Mol. Pharmaceutics* **2022**, *19* (7), 2022−2031.
(26) Brader, M. L.; Williams, S. J.; Banks, J. M.; Hui, W. H.; Zhou, Z. H.; Jin, L. Encapsulation State of Messenger RNA inside Lipid Nanoparticles. *Biophys. J.* **2021**, *120* (14), 2766−2770.
(27) Cheng, M. H. Y.; Leung, J.; Zhang, Y.; Strong, C.; Basha, G.; Momeni, A.; Chen, Y.; Jan, E.; Abdolahzadeh, A.; Wang, X.; Kulkarni, J. A.; Witzigmann, D.; Cullis, P. R. Induction of Bleb Structures in Lipid Nanoparticle Formulations of mRNA Leads to Improved Transfection Potency. *Adv. Mater.* **2023**, *35* (31), No. 2303370.
(28) Whitehead, K. A.; Matthews, J.; Chang, P. H.; Niroui, F.; Dorkin, J. R.; Severgnini, M.; Anderson, D. G. In Vitro−In Vivo Translation of Lipid Nanoparticles for Hepatocellular siRNA Delivery. *ACS Nano* **2012**, *6* (8), 6922−6929.
(29) Paunovska, K.; Sago, C. D.; Monaco, C. M.; Hudson, W. H.; Castro, M. G.; Rudoltz, T. G.; Kalathoor, S.; Vanover, D. A.; Santangelo, P. J.; Ahmed, R.; Bryksin, A. V.; Dahlman, J. E. A Direct Comparison of in Vitro and in Vivo Nucleic Acid Delivery Mediated by Hundreds of Nanoparticles Reveals a Weak Correlation. *Nano Lett.* **2018**, *18* (3), 2148−2157.

https://doi.org/10.1021/acsami.4c20077
ACS Appl. Mater. Interfaces 2025, 17, 3097−3105